TU Delft

Delft University of Technology

Document Version
Final published version

Licence
CC BY-NC-ND

Citation (APA)
Elbertse, R. J. G., Xu, M., Keşkekler, A., Otte, S., & Norte, R. A. (2026). Detection of Microelectromechanical System Acoustics via Scanning Tunneling Microscopy. *ACS Nano*, *20*(28), 20160-20175. https://doi.org/10.1021/acsnano.6c04148

Important note
To cite this publication, please use the final published version (if applicable).
Please check the document version above.

Copyright
In case the licence states “Dutch Copyright Act (Article 25fa)”, this publication was made available Green Open Access via the TU Delft Institutional Repository pursuant to Dutch Copyright Act (Article 25fa, the Taverne amendment). This provision does not affect copyright ownership.
Unless copyright is transferred by contract or statute, it remains with the copyright holder.

Sharing and reuse
Other than for strictly personal use, it is not permitted to download, forward or distribute the text or part of it, without the consent of the author(s) and/or copyright holder(s), unless the work is under an open content license such as Creative Commons.

Takedown policy
Please contact us and provide details if you believe this document breaches copyrights.
We will remove access to the work immediately and investigate your claim.

This work is downloaded from Delft University of Technology.

ACS NANO

Open Access

This article is licensed under CC-BY-NC-ND 4.0

www.acsnano.org

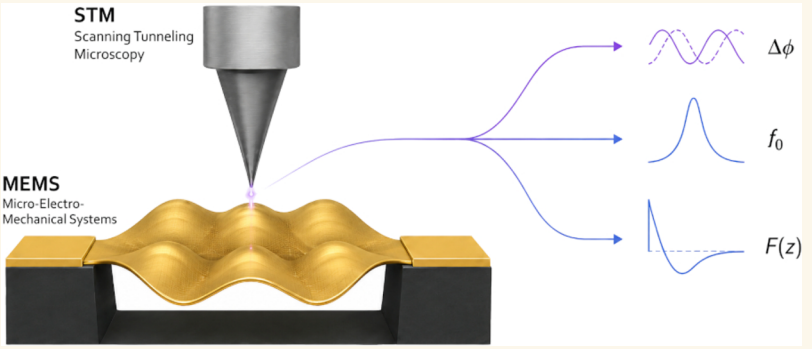
Detection of Microelectromechanical System Acoustics via Scanning Tunneling Microscopy

Robertus J. G. Elbertse,[§] Minxing Xu,[§] Ata Keşkekler, Sander Otte,* and Richard A. Norte*

Cite This: *ACS Nano* 2026, 20, 20160–20175

Read Online

ACCESS | Metrics & More | Article Recommendations | Supporting Information



ABSTRACT: Scanning tunneling microscopy (STM) and microelectromechanical systems (MEMS) traditionally address vastly different length scales—one resolving atomic structure and the other, engineering macroscopic motion. Bridging these regimes is particularly compelling for high-Q membrane resonators operating at cryogenic temperatures, where conventional optical and electrical readout methods introduce dissipation, heating, or electromagnetic loading that perturbs temperature-dependent force measurements. Here, we unite these two fields by using an STM tip as both an actuator and a detector to perform minimally invasive measurements of high-aspect-ratio MEMS resonators. We resolve acoustic modes of millimeter-scale, high-Q membranes with picometer spatial precision, without relying on optical readout or capacitive coupling. Because the tunneling junction is intrinsically localized and dissipates negligible power, the measurement introduces minimal back-action or heating, enabling direct access to the intrinsic dynamics of microgram-mass oscillators. We implement three complementary detection modalities: phase-sensitive homodyne readout, rapid measurements compatible with the STM feedback cycle, and near-nonperturbative operation via controlled tip retraction—that together span a wide range of measurement conditions and enable force sensitivity on the order of a few piconewtons. These approaches establish STM as a broadband, surface-localized nanomechanical detector capable of operating where conventional optical access is impractical, including cryogenic and high-magnetic-field environments. This platform expands the experimental toolbox for nanomechanics, enabling precision measurements of forces, displacements, and pressures in suspended systems—including Casimir interactions and hybrid electromechanical devices—across cryogenic and high-field environments.

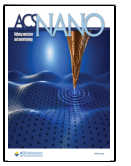
KEYWORDS: *scanning tunneling microscopy, microelectromechanical systems, nanomechanical resonators, near-nonperturbative force sensing, membrane acoustics*

1. INTRODUCTION

High-stress nanomembranes provide exceptional mechanical isolation through dissipation dilution, enabling force sensitivities that approach the quantum regime and access to macroscopic quantum phenomena. Their suspended geometries and large surface areas make them powerful platforms for precision measurements of pressure, acceleration, and Casimir forces.[1] As a result, nanomembranes have become central elements in quantum-limited sensing and force metrology.

Despite their exceptional isolation and force sensitivity, membrane dynamics are typically studied using optical[2−5] or

Received: March 4, 2026
Revised: May 24, 2026
Accepted: May 26, 2026
Published: July 8, 2026



ACS Publications

© 2026 The Authors. Published by American Chemical Society

Downloaded from http://pubs.acs.org/ancac3/article-pdf/20/28/20160/6530070/acsnano.6c04148.pdf by TU DELFT user on 29 July 2026

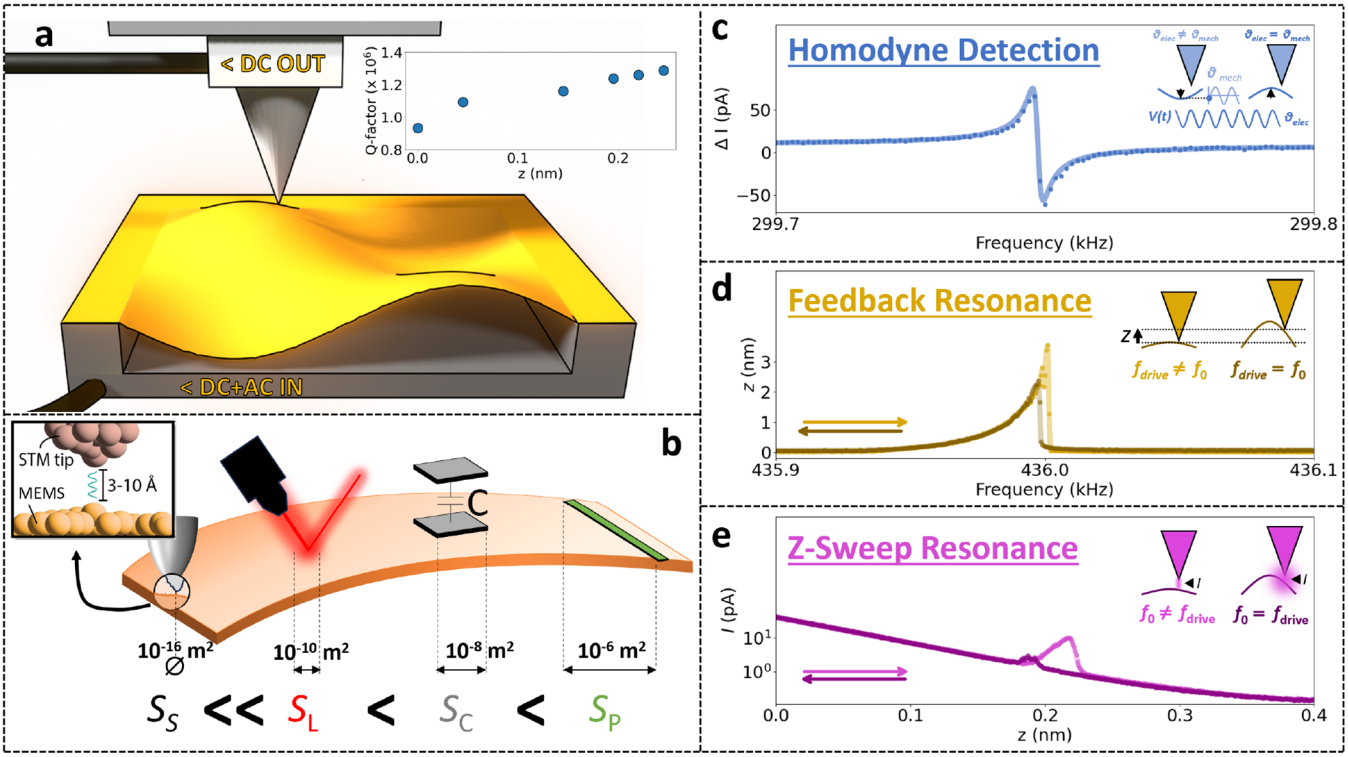


Figure 1. Experimental setup and detection modalities.(a) Schematic of the measurement configuration. A MEMS resonator containing a square superconducting membrane is biased with a combined DC and AC voltage, while an STM tip probes the membrane surface. The oscillating voltage component drives membrane motion (illustrated here in the (2,2) vibrational mode), and the resulting modulation of the tunneling current is converted into a measurable DC signal. The inset on the top right shows the measured *Q*-factor as a function of tip height. (b) Comparison of effective interrogation areas for common membrane motion detection techniques: STM (S_S), optical interferometry (S_L), capacitive sensing (S_C), and piezoelectric detection (S_P), illustrating the nanoscale locality of the STM probe. (c–e) Three complementary measurement modalities. (c) Homodyne detection: Lock-in signal obtained from phase-sensitive tunneling current modulation (light curve shows a Lorentzian fit). (d) Feedback resonance: Tip height as a function of drive frequency under constant-current feedback. (e) Z-sweep resonance: Tunneling current as a function of tip height at a fixed drive frequency. Forward and backward sweeps are indicated by arrow colors.

electrical techniques[6−8] that introduce dissipation, heating, or electromagnetic loading, thereby limiting access to their intrinsic mechanical and electronic properties. While recent scanning probe approaches, including scanning force microscopy on graphene[9] and scanning microwave microscopy on silicon nitride resonators,[10] improve spatial locality, they still rely on optical or microwave excitation for mechanical readout. In contrast, we use the STM tunneling junction itself as a local electromechanical transducer (see Figure 1a) to excite and detect acoustic resonances of suspended (super)conducting membranes, achieving intrinsic sub-Å displacement sensitivity while preserving local electronic characterization.

STM has previously been applied to free-standing graphene membranes, primarily to study and manipulate static deformation, wrinkling, and local electromechanical responses in highly compliant micron-scale systems.[11−20] In these works, the tunneling junction was used to probe or induce local shape modifications rather than to access driven acoustic resonances of suspended mechanical resonators. The approach presented here enables the controlled excitation and detection of acoustic modes in suspended membranes whose masses are several orders of magnitude larger than those previously investigated using STM. By extending tunneling-based transduction into the regime of mesoscopic mechanical dynamics, this framework connects atomic-scale tunneling sensitivity with collective vibrational motion in macroscopic-area membranes.

The electronic configuration follows a conventional STM architecture, requiring only a bias electrode and a current readout. Because the tunneling current depends exponentially on the tip−sample separation, a displacement of approximately 0.15 nm produces a decade change in current under our operating conditions. Rather than using this sensitivity solely for topographic imaging, we repurposed it to detect and drive the acoustic oscillations of suspended membranes. Experimental details such as applied power and tunneling set point are provided in Supporting Information Note 1.

We begin by introducing the STM-based electromechanical transduction scheme and establishing three complementary detection modalities with distinct measurement characteristics for probing the tip−membrane interaction. We develop a quantitative force model incorporating electrostatic and short-range contributions and demonstrate, through bias-dependent measurements analogous to Kelvin-probe spectroscopy, that the approach reproduces established electrostatic behavior. Leveraging STM's inherent spatial selectivity, we map membrane dynamics across microscopic and macroscopic length scales. Finally, operating in the nonperturbative limit, we extract the long-range force curve and demonstrate piconewton-level force resolution.

https://doi.org/10.1021/acsnano.6c04148
ACS Nano 2026, 20, 20160−20175

Downloaded from http://pubs.acs.org/ancac3/article-pdf/20/28/20160/6583007O/acsnano.6c04148.pdf by TU DELFT user on 29 July 2026

2. RESULTS AND DISCUSSION

2.1. STM-Based Electromechanical Transduction

Our membrane samples consist of silicon substrates with deposited metal layers, which are patterned with holes to remove the underlying substrate, leaving behind suspended, high-aspect-ratio membranes. We focus on two types: a more compliant dielectric SiN membrane coated with superconducting NbTiN[21] and a stiffer gold-coated membrane. We attribute the difference in compliance to the gold being deposited via e-beam evaporation, whereas NbTiN is grown by atomic layer deposition (see the Section 8 for more details). We find a Q-factor of over 10^6 for the NbTiN-coated membrane; see Supporting Information Note 2.

To probe their delicate mechanical motion with atomic precision, we use an STM configuration that combines cryogenic operation, ultrahigh vacuum ($\approx 10^{-11}$ mbar), and optical access that enables precise prealignment of the tip−sample junction on a patterned chip. The ultrahigh-vacuum environment minimizes viscous damping, typically difficult to achieve with standard turbo- or rough-pumped systems, thereby enhancing the resolution of the membranes' intrinsic acoustic line widths. Their high tensile stress keeps the membranes taut and stable, enabling reliable high-precision approaches.

Figure 1a outlines the experimental setup. A combined DC + AC voltage is applied between the metallic membrane and the metal STM tip, following

$$V(t) = V_{\mathrm{DC}} + V_{\mathrm{drive}}\sin(2\pi f_{\mathrm{drive}}\, t)$$

where the AC component with amplitude V_{drive} actuates the membrane motion, while the DC offset V_{DC} stabilizes the tunneling current used by the STM feedback loop. The membrane oscillations are not observed in real time because the 1.1 kHz bandwidth of the current preamplifier is far below the membrane's mechanical resonance frequencies, which in this study lie between 100 kHz and 1 MHz. Instead, we detect the motion indirectly, as further explained below. Using a nested feedback loop to maintain a stable tip current, we also maintain lateral precision down to the picometer scale. As shown later (Figure 4a,b), this positional stability is essential for reproducibility, since even subnanometer-scale lateral shifts in tip position alter the local tip−membrane coupling strength. This requirement arises from the STM's exceptionally small effective interrogation area, set by the short-range nature of electron tunneling and near-field tip−sample forces, which is expected to be on the order of $S_{\mathrm{S}} \approx 10^{-16}$ m^2 (see Section 11.3 of ref 22). As illustrated in Figure 1b, this nanoscale interrogation window distinguishes our approach from other membrane readout techniques such as optical interferometry (typical spot $S_{\mathrm{L}} \approx 10^{-10}$ m^2[22−4]), capacitive sensing ($S_{\mathrm{C}} \approx 10^{-8}$ m^2[6,8,23]), or piezoelectric detection ($S_{\mathrm{P}} \approx 10^{-6}$ m^2[24,25]). The STM thus accesses a spatially localized regime of membrane dynamics unattainable by macroscopic probe geometries.

This localized measurement also imparts limited back-action on the membrane, as evidenced by the high mechanical quality factor ($Q \sim 10^6$) and its increase with tip−sample separation (Figure 1a, inset), demonstrating that the STM-induced dissipation remains limited, especially as the tip is retracted further. Local heating is also much smaller, with typical values of 10 pA and 50 mV for DC tunneling (0.5 pW). This is orders of magnitude smaller than competing methods, such as lasers that use >10 μW,[2−6,9,26] a portion of which is converted into local heating, or capacitive coupling at 0.1 μW[7,27] and piezoelectric readout at 1 μW.[28] While the injected driving power, typically around −50 dBm (10nW), is substantially higher, this is most likely dissipated throughout the entire membrane rather than locally at the measurement point. By introducing so little heat, one can maintain, for example, superconductivity, which the STM can even measure directly as it has access to the electronic properties of the membrane (see Supplementary Note 3).

We explore three modalities of this measurement technique, illustrated in Figure 1c−e: homodyne detection (c, blue), feedback resonance (d, yellow), and z-sweep resonance (e, pink). Each modality relies on aligning the driving frequency f_{drive} with the resonance frequency of the membrane, f_0. In the first two modalities, this is accomplished by sweeping f_{drive} while monitoring the response signal, whereas in the last modality, it is f_0 that is indirectly swept under a constant f_{drive}.

In the case of homodyne detection, the response corresponds to the difference in tunneling current between measurements with and without the oscillating voltage. This is achieved by chopping the excitation at a reference frequency f_{LI} well below the preamplifier cutoff and then demodulating the resulting signal at this same frequency. This yields a lock-in signal that carries phase information (see Supplementary Note 4 for more details) and is inspired by recent ESR-STM experiments, operating at GHz frequencies.[29] This lock-in signal scales approximately linearly with the driving amplitude and therefore imposes a lower limit to the usable drive power. Homodyne detection mixes the oscillating tunneling conductance, arising from membrane motion, with the applied AC bias, producing a phase-sensitive DC signal that enables direct measurement of the mechanical phase at subpicometer amplitudes. The resulting signal scales as $\cos(\vartheta_{\mathrm{elec}} - \vartheta_{\mathrm{mech}})$, where $\vartheta_{\mathrm{mech}}$ denotes the phase of the membrane motion and $\vartheta_{\mathrm{elec}}$ is the phase of the electrical drive (see Figure 1c). This DC component is further enhanced by the exponential dependence of the tunneling conductance on the tip−membrane distance (see Supplementary Note 4). Combined with lock-in detection that suppresses out-of-band noise, this enables robust phase-sensitive readout of the membrane motion. Figure 1c shows the lock-in signal, after rejecting the capacitive background via phase adjustment, measured on a stiff gold-coated membrane.

In more compliant membranes, such as those coated with NbTiN, the mechanical oscillation amplitudes can easily reach the nanometer scale and beyond. As the driving frequency f_{drive} approaches the membrane's resonance frequency f_0, the membrane motional amplitude increases. This in turn reduces the effective tip−membrane distance, causing an increase in time-averaged tunneling current. The constant-current feedback loop then retracts the tip to maintain a stable time-averaged current, and we therefore take the tip height as the response signal in the feedback resonance modality. The abrupt drop shown in Figure 1d occurs when f_{drive} exceeds f_0, and this also reflects a softening response, as discussed later. When sweeping f_{drive} downward, a sudden jump appears instead. Provided that the feedback is sufficiently fast, a tip crash is avoided despite the sudden multinanometer oscillation amplitude. We note that the sudden drop shown during this modality also occurs in the membrane's linear regime (see Supplementary Note 5).

The Z-sweep resonance modality inverts the logic of feedback resonance. Instead of sweeping the driving frequency,

Downloaded from http://pubs.acs.org/ancac3/article-pdf/20/28/20160/6530070/acsnano.6c04148.pdf by TU DELFT user on 29 July 2026

https://doi.org/10.1021/acsnano.6c04148
ACS Nano 2026, 20, 20160−20175

Table 1. Comparison of STM-Based Membrane Resonance Detection Modalities[a]

Parameter	Homodyne Detection	Feedback Resonance	Z-Sweep Resonance
Key advantage	Provides phase information	Quickest, safest modality	Reaches non-perturbative limit
Signal	ΔI (pA)	z (nm)	I (pA)
Mech. Amplitude Range	sub-pm to nm-scale	several pm to nm-scale	several pm to nm-scale
Drive Power Range	-60 dBm to -20 dBm	-110 dBm to -20 dBm	-90 dBm to -40 dBm
Operational complexity	Requires lock-in detection and signal chopping	None	Requires reference measurement
Uses STM feedback	✓	✓	—
Sweeps f_{drive} / f_0	f_{drive}	f_{drive}	f_0
Additional feature	Yields side peaks	Can determine stiffness stability	Allows determining long-distance force curve

[a]The three modalities are compared according to their key advantages, transduced physical quantity, mechanical amplitude range (minimum value also describes displacement resolution), drive power range (as shown in this work, actual range may be larger), operational complexity, status of the STM feedback loop, method of frequency interrogation (drive sweep versus resonance sweep), and additional distinguishing features.

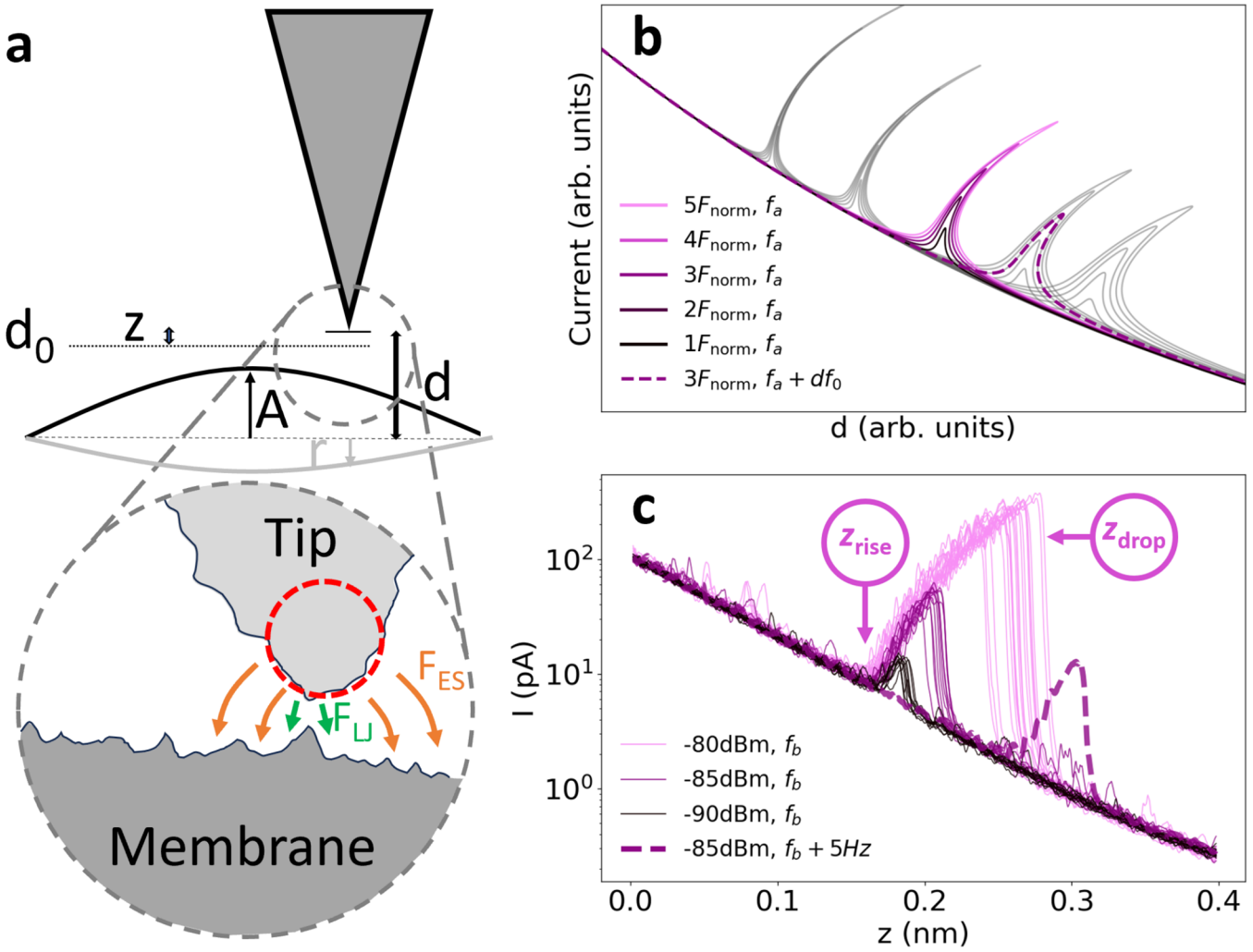


Figure 2. Force model, simulated response, and experimental nonlinear behavior. (a) Schematic of the force model describing the tip−membrane interaction. The Lennard-Jones force (F_{LJ}) and electrostatic force (F_{ES}) are indicated, along with the membrane oscillation amplitude A, the instantaneous tip−membrane distance d, an offset distance d_0, the displacement variable z, and the membrane position coordinate r. The red circle indicates the spherical approximation of the STM tip. (b) Simulated tunneling current as a function of tip−membrane distance for multiple driving frequencies (see Section 8). The frequency-dependent response produces tilted current maxima at distinct tip heights. For each frequency, simulations are repeated for several driving powers P (legend). Selected simulation traces are highlighted for clarity. (c) Experimental tunneling current measured on an NbTiN membrane as a function of tip displacement z at a driving frequency of 278.61 kHz for several powers, together with a measurement at 278.615 kHz and −85 dBm. The data exhibit power-dependent shifts in the current maxima, defining z_{drop}, while z_{rise} is virtually independent of power.

Downloaded from http://pubs.acs.org/ancac3/article-pdf/20/28/20160/6530070/acsnano.6c04148.pdf by TU DELFT user on 29 July 2026

https://doi.org/10.1021/acsnano.6c04148
ACS Nano 2026, 20, 20160−20175

the tip height z is varied, while the feedback loop is disabled, and the tunneling current is recorded. As the tip is retracted and the tunneling current decreases exponentially, the forces imparted by the tip on the membrane decrease and the resonance frequency f_0 goes up. Then, when the membrane's resonance frequency approaches the fixed driving frequency f_{drive}, the membrane oscillation amplitude increases sharply and enhances the current. This produces a characteristic rise in current at a well-defined height z_{rise}. Once the tip is moved beyond the maximum oscillation amplitude, the system abruptly switches to a lower-amplitude steady state, leading to a sudden drop in current. This behavior reflects the nonlinear softening response of the membrane, as explored later.

In a reverse sweep (i.e., with decreasing tip height), only a minor current increase is observed, consistent with the hysteresis expected for a softening resonator. This modality can be applied with the tip positioned several nanometers above the surface, which minimizes tip−membrane interaction. However, the absence of the feedback loop's automatic retraction makes it more susceptible to tip crashes if operated at excessive driving power, and additional steps may be required for proper interpretation of results.

Table 1 summarizes the main differences in applicability between the three detection modalities. Homodyne detection is preferred when phase information is required, for instance, to determine whether the oscillating electric field locally pushes or pulls the membrane, to verify that the electrical coupling between the tip and membrane is stable, or to identify whether the response remains in the linear regime. Feedback resonance is the most suitable when measurements need to be performed rapidly, such as during limited cryogenic hold times, or when tracking the resonance frequency efficiently as it shifts under changing external conditions. For example, in our related work where we measure the Casimir force across the membrane's superconducting transition,[1] we required low driving powers and a fast and reliable measurement modality to overcome our limited liquid helium hold time at elevated temperatures, thus making feedback resonance a natural choice. Z-sweep resonance, on the other hand, is the method of choice when one aims to minimize the influence of the STM tip on the membrane altogether and measure its intrinsic mechanical response as the tip moves several nanometers away from the membrane to reduce direct tip−membrane interaction.

Each modality operates within a characteristic range of oscillation amplitudes and driving powers. Because the homodyne signal amplitude scales linearly with V_{drive}, it will not work for driving powers less than −60, but it amplifies even sub-pm oscillations. In contrast, the feedback and Z-sweep resonance modalities require oscillation amplitudes exceeding a few picometers to produce measurable responses. Our gold-coated membrane did not yield sufficiently high mechanical oscillation amplitudes, thereby limiting the applicable modality on this membrane to homodyne detection. The driven power range shown in Table 1 is based only on the limits explored in this work and may be stretched to larger powers if one takes additional safety precautions.

Furthermore, homodyne detection requires the excitation signal to be chopped and demodulated at the lock-in frequency f_{LI} for acquiring a signal that overcomes the noise (see Supporting Information Note 4 for more details). To achieve this sufficient signal-to-noise ratio, this method is slower than feedback resonance and slightly more technically involved. Interestingly, this same chopping introduces side peaks of the resonance at $f_i = f_{drive} + (1 + 2i)f_{LI}$, which may be used to help find the resonance frequencies. Feedback resonance, in contrast, can reveal stiffness instabilities by identifying conditions under which the tip transitions between two metastable states (see Supporting Information Notes 5 and 7). Finally, as shown in the inset of Figure 1a, and also as shown in Supporting Information Note 2, when the tip is placed further away, a higher Q-factor is attained, suggesting less tip-induced damping. Taking this limit to the extreme, Z-sweep resonance uniquely probes the nonperturbative limit and can map the full force curve as the tip retracts, as illustrated in Figure 5.

In summary, each of the three modalities presented here offers distinct advantages and operating regimes.

3. FORCE MODEL FOR TIP−MEMBRANE INTERACTION

We now examine the fundamental forces between the STM tip and the membrane, predominantly the Lennard-Jones force F_{LJ} and the force derived from the electrostatic potential F_{ES} (Figure 2a). For a full mathematical description, please see the Section 8. Here, we will focus on a more qualitative description.

In the linear regime, the unperturbed membrane behaves as a harmonic oscillator of stiffness k, while the STM tip introduces an additional nonlinear interaction potential. The combined potential $U(r)$ gives rise to an effective force $F(d, V_{DC}) = -\partial U/\partial d$, which depends on both the tip−membrane separation d and the applied bias voltage V_{DC}. The curvature of this interaction potential modifies the effective restoring force of the membrane and therefore shifts its resonance frequency, providing an experimentally accessible probe of the tip−membrane interaction.

$$F(d,\ V_{DC}) = 4\epsilon_{LJ}\left[-12\left(\frac{\sigma^{12}}{d^{13}}\right) + 6\left(\frac{\sigma^{6}}{d^{7}}\right)\right] - \frac{C_1 V_{DC}^2}{d^{p}} \tag{1}$$

while the associated frequency shift can be expressed as

$$\Delta f^2 = \frac{1}{4\pi^2}\left[\frac{4\epsilon_{LJ}}{m}\left(\frac{156\sigma^{12}}{d^{14}} - \frac{42\sigma^{6}}{d^{8}}\right) - \frac{pC_1 V_{DC}^2}{m d^{p+1}}\right] \tag{2}$$

Here, ϵ_{LJ} is the energy coefficient, m is the modal mass, σ is the distance parameter, d is the distance between the tip and the equilibrium position of the membrane, and C_1 is the effective electrostatic coupling constant between the tip and the membrane; $1 \le p \le 2$ depends on the exact tip shape (i.e., to what extent the red circle approximates the tip well in Figure 2a). Furthermore, d is the actual tip−membrane distance, while z is a relative measure from an initial starting point d_0, based on an initial conductance: $d = z + d_0$.

We will show how this model applies to the results obtained with the Z-sweep resonance, as this modality uniquely offers a view into the entire force curve. Numerical simulations (see Figure 2b) using this model reproduce the nonlinear response observed experimentally (see Figure 2c) with the Z-sweep resonance modality. Here, we increase the drive power from F_{norm} to $5 \times F_{norm}$, where F_{norm} is a normalized force qualitatively determined to be at the onset of nonlinear frequency response. The increased drive power amplifies nonlinear response, producing canted peaks characteristic of

Downloaded from http://pubs.acs.org/ancac3/article-pdf/20/28/20160/6530070/acsnano.6c04148.pdf by TU DELFT user on 29 July 2026

https://doi.org/10.1021/acsnano.6c04148
ACS Nano 2026, 20, 20160−20175

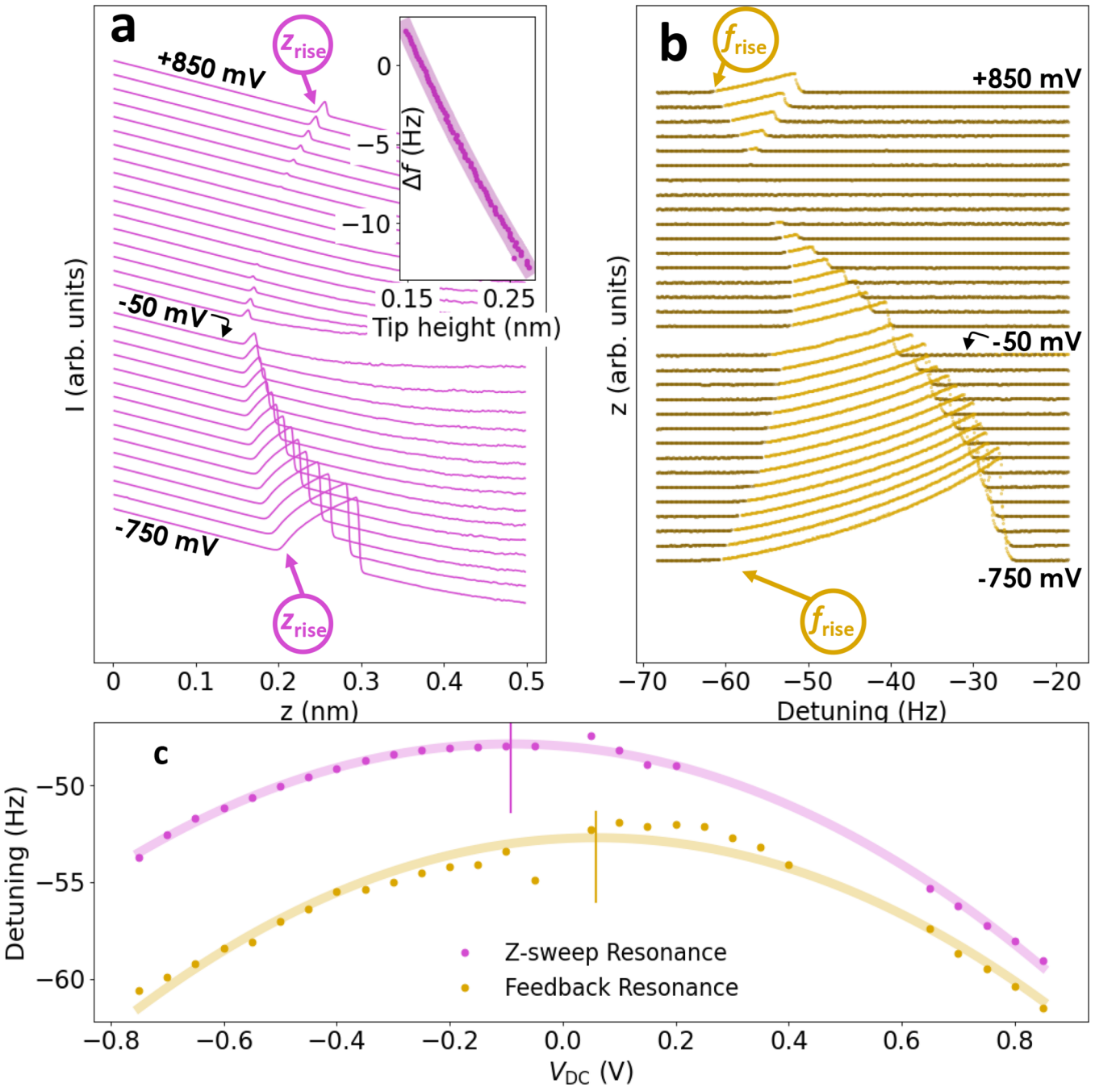


Figure 3. Determination of the local contact potential difference. (a) Z-sweep resonance measurements showing tunneling current as a function of tip displacement z for different bias voltages V_{DC}. The curves are vertically offset for clarity. The tip height at which the current begins to increase defines z_{rise}. Inset: Mapping between tip displacement and frequency shift (see text), allowing conversion of z_{rise} to the corresponding resonance frequency f_{rise}. (b) Feedback resonance measurements showing tip height as a function of drive frequency f_{drive} for different V_{DC} values. Curves are vertically offset for clarity. The frequency at which the tip height increases defines f_{rise}. (c) Detuning of the resonance frequency extracted from panels (a) and (b) as a function of V_{DC}, together with parabolic fits. The fits yield a local contact potential difference of −92.6 ± 4.3 mV for the Z-sweep resonance modality and +58.3 ± 10.4 mV for the feedback resonance modality. The reference frequency f_0^* used to determine detuning is obtained from the fit shown in Figure 5a.

nonlinear softening (see the Section 8 for more details). The experimental data in Figure 2c show the corresponding behavior, including a sudden drop in current as the system transitions to a lower-amplitude steady state. We note that occasional switching between these states (see Supplementary Note 6) confirms the presence of bistability typical of softening resonators.

For these softened peaks, accurately determining the exact value of z_0, the tip height where the resonance frequency precisely matches the driving frequency, can be challenging. However, as shown in Figure 2c, since z_{rise}, the tip height during tip retraction where the current starts to increase, is relatively stable across driving power, while z_{drop}, the tip height during tip retraction where the current suddenly drops, is less consistent, we approximate $z_0 \approx z_{rise}$. To determine the actual

https://doi.org/10.1021/acsnano.6c04148
ACS Nano 2026, 20, 20160−20175

Downloaded from http://pubs.acs.org/ancac3/article-pdf/20/28/20160/6530070/acsnano.6c04148.pdf by TU DELFT user on 29 July 2026

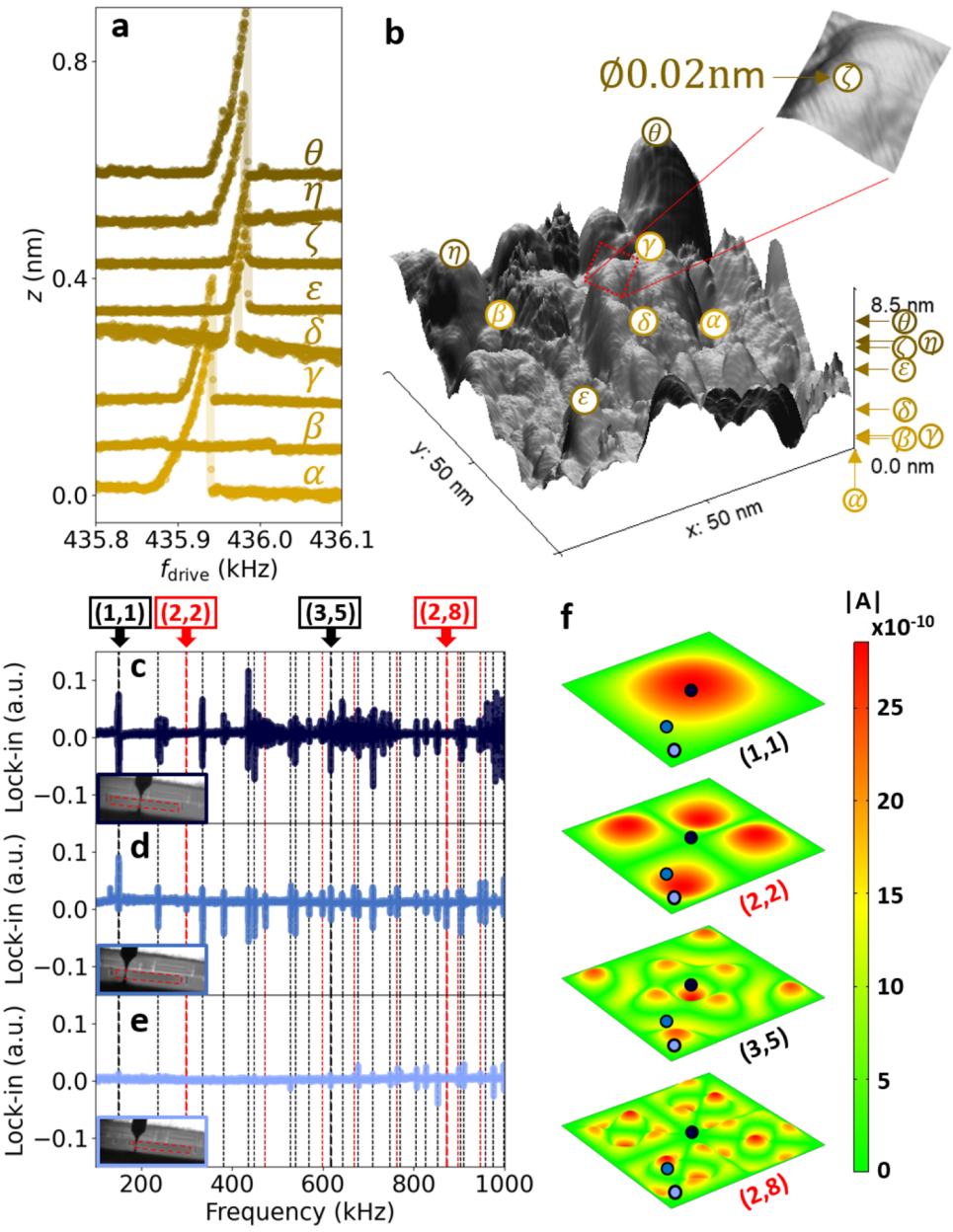


Figure 4. Lateral dependence of membrane resonance measurements. (a) Feedback resonance measurements acquired at different lateral tip positions indicated in panel (b) and labeled with corresponding Greek letters. Curves are vertically offset for clarity. (b) Three-dimensional topographic image of the membrane surface showing the measurement locations used in panel (a). The vertical axis represents the off-resonance tip height. Inset: Zoom-in demonstrating positional stability of approximately 0.02 nm during measurement. (c) Homodyne detection spectra acquired between 100 and 1000 kHz on the gold-coated membrane at a fixed lateral position. The fundamental (1,1) mode at 150 kHz is indicated. Vertical dashed lines mark the calculated frequencies of higher-order modes; red lines indicate modes not observed experimentally. Inset: Optical image of the STM tip position. (d, e) Homodyne detection spectra acquired at two additional lateral tip positions (see panel f). (f) Finite-element simulations of selected vibrational modes of a square membrane. The color scale indicates the absolute displacement amplitude. Colored markers denote the corresponding tip locations used in panels (c)−(e).

resonance frequency f_0, especially as it varies with other parameters, a more sophisticated analysis is necessary, as illustrated in the next section.

In summary, the combined Lennard-Jones and electrostatic interaction provides a quantitative framework linking tip−membrane distance to resonance frequency shifts, explains the observed nonlinear softening behavior, and identifies z_{rise} as a robust experimental proxy for tracking resonance conditions in subsequent measurements.

4. ELECTROSTATIC FORCES

The last term in eq 2 is determined by the electrostatic force and scales quadratically with V_{DC}. Varying this potential allows extraction of the local contact potential differential (LCPD) V_{LCPD} using either the z-sweep or the feedback resonance modalities. This approach is analogous to Kelvin-probe measurements in AFM,[30] where V_{DC} compensates for the chemical potential offset between the tip and the membrane. Figure 3a shows the z-sweep resonance curves at different V_{DC} values. As $|V_{DC}|$ increases, the onset of current rise z_{rise} shifts to

https://doi.org/10.1021/acsnano.6c04148
ACS Nano 2026, 20, 20160−20175

Downloaded from http://pubs.acs.org/ancac3/article-pdf/20/28/20160/6583007O/acsnano.6c04148.pdf by TU DELFT user on 29 July 2026

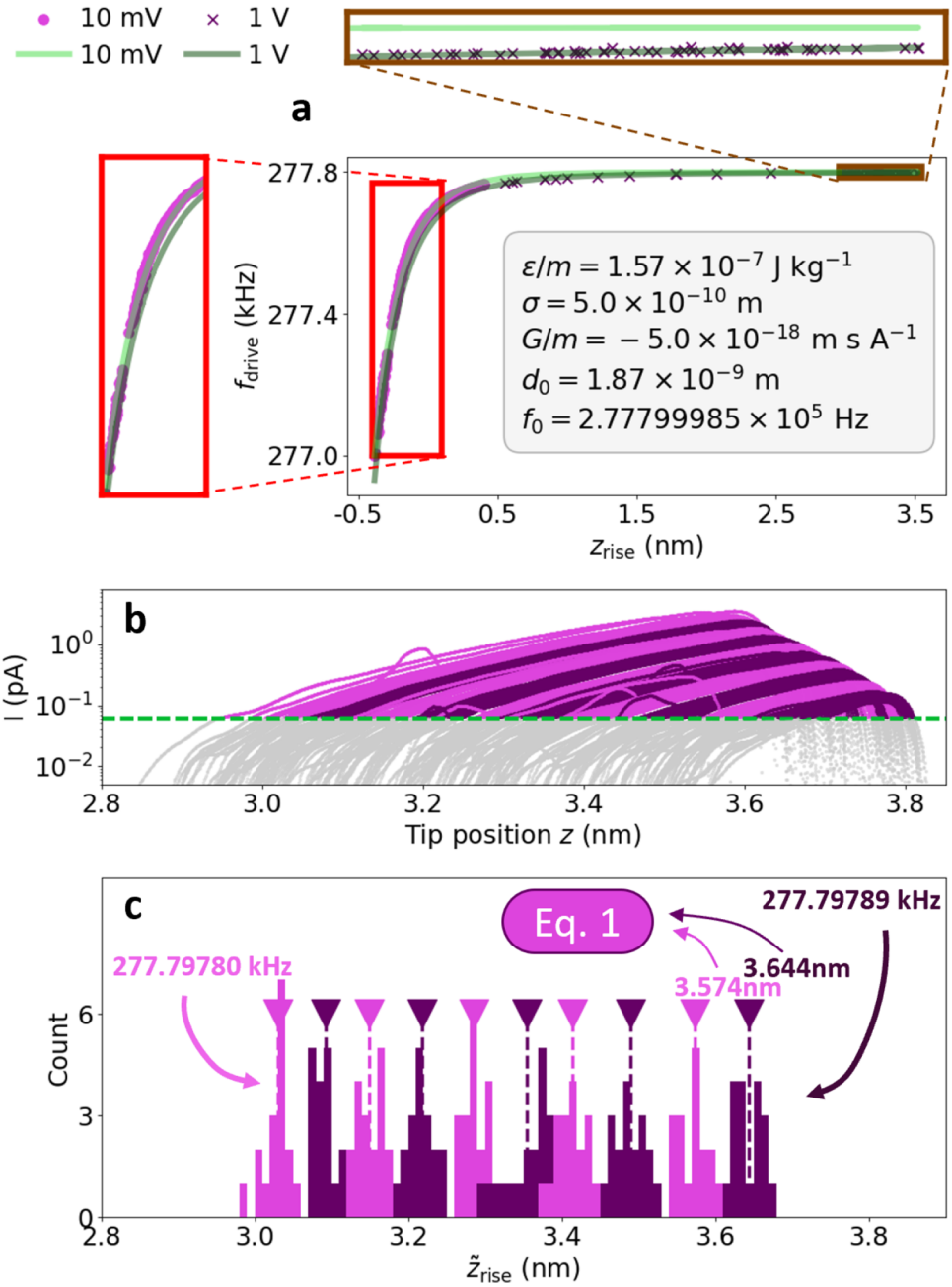


Figure 5. Long-range frequency sensitivity and force resolution. (a) Resonance frequency as a function of tip position z_{rise} over a 4 nm range, measured at V_{DC} = 10 mV (circles) and V_{DC} = 1 V (crosses). Independent fits to eq 2 are shown for each bias. Insets enlarge the low- and high-distance regimes used for fitting. (b) Repeated Z-sweep measurements acquired at ten closely spaced drive frequencies (10 mHz steps), with 20 repetitions per frequency. The tunneling current is plotted as a function of tip position z. The green dashed line indicates the threshold used to determine $\tilde{z}_{rise}$. (c) Histograms of $\tilde{z}_{rise}$ extracted from the data in panel (b). Triangles denote the mean value of each distribution. Using the difference in $\tilde{z}_{rise}$ between the two highest frequencies and eq 1, the corresponding detectable force difference is approximately 6 pN.

larger tip−membrane distances, indicating that the electrostatic attraction modifies the resonance frequency f_0. Converting these z_{rise} values using a height-to-frequency mapping (inset) yields a parabolic dependence of frequency detuning on bias (panel c), characteristic of LCPD behavior. The mapping in the inset was made by finding z_{rise} in repeated Z-sweep resonance measurements at different f_{drive} values.

A similar trend appears for the feedback resonance data in Figure 3b, where the resonance frequency f_0 is estimated with the onset of the tip retraction f_{rise} during upward frequency sweeps. Both modalities reproduce the expected LCPD parabolas (panel c), with Z-sweep resonance offering higher precision (uncertainty is less than half) but requiring additional acquisition steps. The detuning shown in the axes of panels b and c is with respect to f_0^*, which corresponds to the resonance in the absence of the tip, discussed later. We note that, as shown in Supplementary Note 8, when the tip is brought closer (i.e., at a larger set point current), the LCPD parabola becomes steeper.

https://doi.org/10.1021/acsnano.6c04148
ACS Nano 2026, 20, 20160−20175

Downloaded from http://pubs.acs.org/ancac3/article-pdf/20/28/20160/6583070/acsnano.6c04148.pdf by TU DELFT user on 29 July 2026

5. SPATIAL MAPPING OF MEMBRANE RESONANCES

Having established the electrostatic contribution to the tip−membrane interaction, we next examined how this coupling varies spatially across the membrane. These measurements serve two purposes: first, they demonstrate the exceptional positional reproducibility of the STM-based approach, allowing us to return to the same nanoscopic position, even to the level of individual surface atoms. Second, they allow us to assess the uniformity of the mechanical and electrical responses across both microscopic and macroscopic length scales. This spatial validation provides the foundation for the subsequent exploration of the full interaction potential toward the nonperturbative limit.

The resonance frequencies of the membrane vary laterally on the microscopic scale, primarily because the STM tip samples slightly different effective tip−membrane distances as it moves across the surface topography at constant current. Figure 4a shows the feedback resonance measurements performed at several positions in close proximity to each other on a NbTiN membrane (locations marked in panel b). Even lateral shifts of only a few nanometers produce distinct resonance frequencies and amplitudes. This sensitivity reflects how local topographic variations lead to measurable changes in the tip−membrane coupling. We found, in general, an increase in resonance frequency when the tip is positioned at a higher absolute position. However, this dependence is not strictly monotonic due to the irregular and unknown shape of the tip (i.e., Figure 2a zoom-in is highly idealized). Likewise, a stronger response is typically found at local height maxima. Both observations are consistent with the tip being further away from the bulk of the membrane. To reach these local maxima, we employ nested "top-of-hill" feedback routines that keep the tip centered on such a height maximum, allowing positional stability on the order of ≈0.02 nm (see Figure 4b inset). Maintaining the membrane interrogation position with such precision is one of the key aspects that sets this STM-based method apart.

On larger length scales, the position dependence reflects the membrane's global vibrational mode structure rather than local topography. To explore this regime, we employ homodyne detection on a gold-coated membrane, whose low compliance suppresses large oscillation amplitudes. This allows us to apply strong driving forces and perform stable, wide-range frequency sweeps without risking tip−membrane contact. Figure 4c−e displays representative lock-in responses obtained with the STM tip positioned at the membrane center, at an intermediate location, and near a corner (see insets). The spectra span 100−1000 kHz and show multiple resonances corresponding to higher-order mechanical modes.

Using the fundamental (1,1) mode at $f_{1,1}$ = 150 kHz as a reference, the expected frequencies of higher modes are

$$f_{i,j} = f_{1,1}\frac{\sqrt{i^2 + j^2}}{2}$$

Vertical dashed lines in the spectra mark these predicted mode positions. Because the STM probes a single location, it measures the local displacement amplitude $A_{i,j}(x,y)$ of each global mode (i,j) at tip position (x,y) and thus detects a peak only when the tip sits at a position where that mode exhibits appreciable displacement (i.e., away from a node). This explains, for example, why modes with center nodes (e.g., (2, 2) or (2, 8)) vanish when the tip is at the center and why corner placement suppresses modes whose displacement is concentrated toward the membrane interior. Finite-element simulations (COMSOL Multiphysics) in Figure 5f confirm this spatial selectivity, implying we can position our tip so as to access specific modes only.

These results show that STM-based actuation and readout provide a localized probe of membrane motion: small lateral shifts change the effective tip−membrane coupling, and deliberate repositioning maps the modal landscape. In contrast to optical or capacitive readout, the STM tip probes membrane motion at a single nanoscale location, effectively selecting a point within a global modal landscape rather than measuring the spatially averaged dynamics.

6. LONG-RANGE SENSITIVITY AND FORCE RESOLUTION

Having shown that small lateral displacements alter the local coupling strength, we now examine how the same coupling evolves with a vertical displacement. Here, we capture the transition from the perturbative domain, where the tip−membrane interaction noticeably shifts the resonance frequency, to the nonperturbative limit, where the membrane remains driven but oscillates at its intrinsic resonance with only minute frequency shifts. We will then translate these into measurable force differences. This regime enables a form of force metrology in which the STM tip approaches a nonperturbative probe, allowing forces to be quantified while leaving the membrane dynamics essentially unaltered.

The long-range dependence of resonance frequency on tip−membrane separation is shown in Figure 5a, covering a displacement range of nearly 4 nm, acquired using the Z-sweep resonance modality. At large separations, the membrane approaches its unperturbed resonance frequency f_0^* and the curve asymptotically flattens. This behavior reflects the decay of both the Lennard-Jones and electrostatic forces with distance, as described by eq 1. In Figure 5a, two sets of data appear: measurements taken at V_{DC} = 10 mV (circles) and at V_{DC} = 1 V (crosses). The low bias data are used for small tip−membrane separations to avoid preamplifier saturation, whereas the higher bias is required at larger separations to maintain sufficient signal-to-noise. Because the electrostatic force scales as V_{DC}^2, the two bias conditions produce slightly different frequency−distance curves. For clarity, separate fits to eq 2 are shown for each bias (light- and dark-green curves), using identical Lennard-Jones parameters (shown in the figure) but different values for V_{DC}. Both fits reproduce their respective data ranges well and together describe the full long-range behavior.

We note that the fit returns an apparent offset d_0 = 1.87 nm, which exceeds typical static STM tunneling gaps. We interpret this offset as arising from time-averaging over fast, thermally populated nonresonant membrane motion, due to the low bandwidth of the current readout (≲1.1 kHz) compared to the membrane mode frequencies (≳ 100 kHz). This contrasts with our electrically driven resonant measurements; however, in both cases, the majority of the tunneling current flows near the point of maximum membrane extension (see Supplementary Note 9 for details).

In the nonperturbative limit (i.e., large z), the frequency−distance curve approaches an asymptote, and its slope df/dz becomes very small. A small shift in resonance frequency therefore maps onto a large change in effective tip height. In the nonperturbative limit, the flattening of the frequency−

Downloaded from http://pubs.acs.org/ancac3/article-pdf/20/28/20160/6530070/acsnano.6c04148.pdf by TU DELFT user on 29 July 2026

https://doi.org/10.1021/acsnano.6c04148
ACS Nano 2026, 20, 20160−20175

Table 2. Comparison of STM-Based Readout with Common Membrane Detection Techniques[a]

method	eff. area (m^2)	back-action mechanism	sensing dissipation power	cryo/B-field compatibility	applicable surfaces
STM (this work)	10^{-16}	Tip−membrane forces (tunneling, electrostatic)	0.5 pW	excellent	conductive
optical interferometry	10^{-10}	optical heating, radiation pressure	10 μW	limited by laser heating	optically accessible
capacitive sensing	10^{-8}	electrostatic loading	0.1 μW	good	conductive (or metallized)
piezoelectric detection	10^{-6}	built-in transduction	1 μW	good	piezoelectric material (or integrated)

[a]The effective interrogation area is given as an order-of-magnitude estimate for each method.

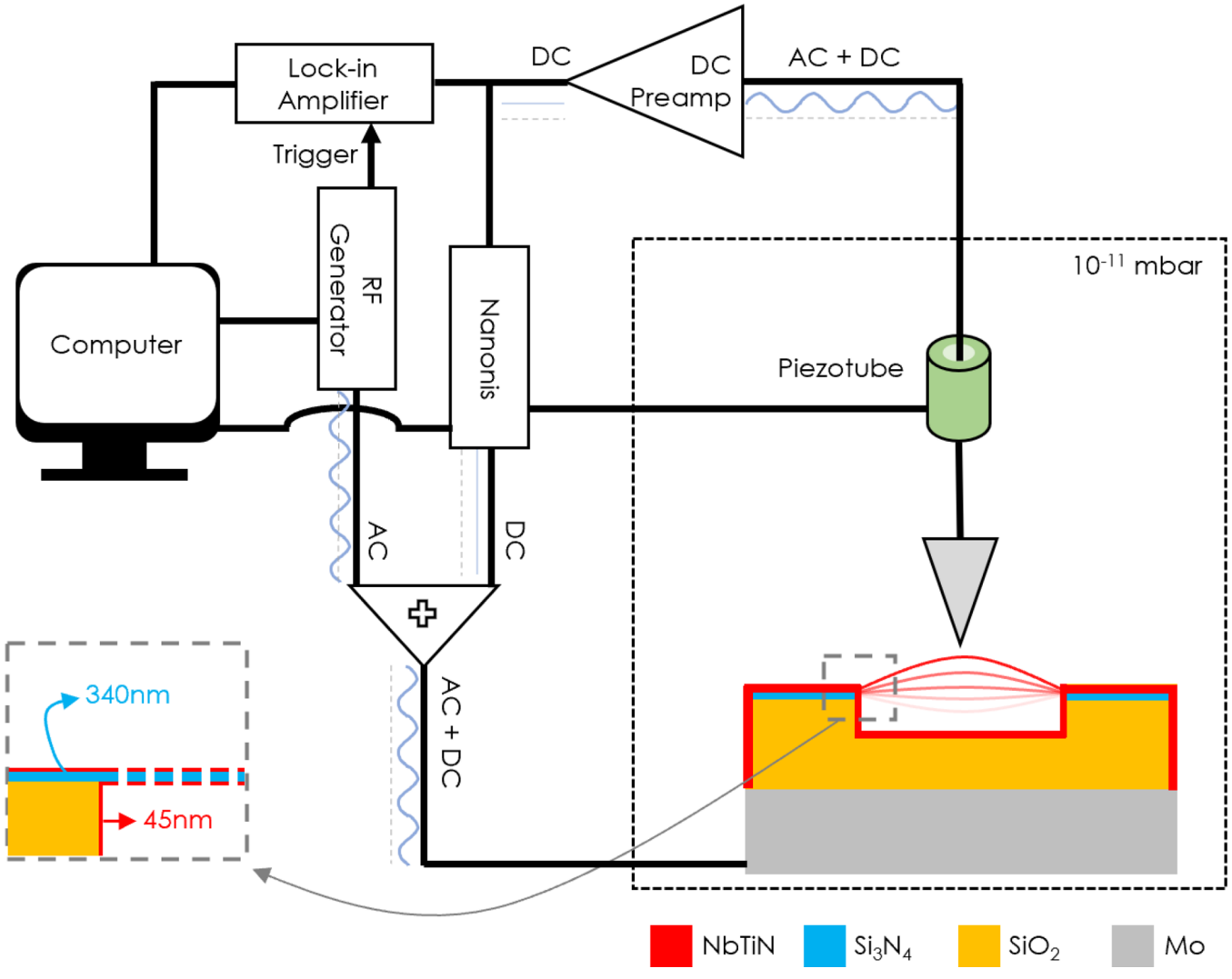


Figure 6. Schematic of the STM-based actuation and readout system. The STM operating system applies a DC bias voltage to the membrane chip, while the tunneling current measured by the STM tip is used for constant-current feedback control of the piezo tube. An RF generator provides an additional AC excitation, combined with the DC bias through a bias tee, to drive membrane motion. Although the tunneling current contains a high-frequency component at the drive frequency, the current preamplifier bandwidth suppresses this component, yielding a DC output for feedback. For homodyne detection, the RF generator output is amplitude-modulated and synchronized with a lock-in amplifier at a frequency below the preamplifier cutoff. All electronic components interface with the computer for control and data acquisition. See the text for more details.

distance curve amplifies small frequency shifts into large effective distance changes, transforming resonance tracking into an ultrasensitive probe of weak forces. In principle, this makes the onset position z_{rise} an extremely sensitive proxy for minute force variations. However, the exact position of z_{rise} cannot be determined experimentally because it occurs below the measurement noise floor. Instead, we define the quantity $\tilde{z}_{rise}$ as the tip height at which the tunneling current exceeds approximately 60 fA as a proxy for z_{rise}. This threshold, which just exceeds the noise floor, is shown as the green dashed line in Figure 5b; see Supplementary Note 10 for more details. To quantify the sensitivity, Figure 5b shows a representative zoom of the high-z tail ($z_{rise} \gtrsim 2.8$ nm), corresponding to the rightmost portion of Figure 5a, where the force curve becomes

https://doi.org/10.1021/acsnano.6c04148
ACS Nano 2026, 20, 20160−20175

Downloaded from http://pubs.acs.org/ancac3/article-pdf/20/28/20160/6583007O/acsnano.6c04148.pdf by TU DELFT user on 29 July 2026

nearly horizontal. For each drive frequency (stepped in 10 mHz increments), the figure shows 20 repeated measurements. The resulting distribution of $\tilde{z}_{rise}$ values, shown in Figure 5c, reveals narrow histograms, demonstrating that frequency differences as small as 10 mHz can be robustly resolved.

This frequency precision can be converted into a force sensitivity by evaluating the force difference between two closely spaced tip−membrane distances. Using eq 1 and the two $\tilde{z}_{rise}$ clusters in Figure 5b that correspond to the largest tip separation (3.574 and 3.644 nm), we obtain a measurable differential force of approximately 6 pN (see Supplementary Note 11 for details).

While the present implementation already yields picogram-level sensitivity, further improvements are achievable. Operating closer to the nonperturbative limit (lower V_{DC}), increasing integration time, or employing a higher-gain current preamplifier would reduce the effective noise floor. For example, repeating these measurements at 10 mV bias, rather than 1 V, which yields a stronger electrostatic force gradient, would lower the calculated force resolution to ∼50 fN. Higher-Q modes or cryogenic optimization could reduce this figure further.

Together, the long-range frequency map and its asymptotic tail demonstrate that STM-based membrane actuation, when operated in the nonperturbative limit, enables extremely sensitive detection of tip-induced forces, which may be used to quantify external forces.

7. CONCLUSIONS

We demonstrate that a cryogenic STM junction can function as a localized electromechanical transducer for suspended nanomembranes, simultaneously driving and detecting mechanical resonances through controllable tip−membrane forces. By tuning these interactions with an external electrical drive, the STM enables stable, minimally perturbative measurements across multiple operating modalities while preserving the intrinsic dynamics of high-stress mechanical resonators. Combined with nanometer-scale positional control, this approach extends tunneling-based sensing from atomic-scale imaging to the characterization of mesoscopic mechanical motions.

The complementary use of homodyne detection, feedback resonance, and z-sweep resonance establishes a unified measurement framework that accesses phase-sensitive response, rapid resonance tracking, and near-nonnegative perturbative operation within a single platform. Together, these capabilities enable spatially localized studies of membrane acoustics and electromechanical coupling in regimes where conventional optical or capacitive readout introduces dissipation, heating, or electromagnetic loading. STM-based transduction therefore provides a practical route toward probing mechanical and electronic phenomena in cryogenic and high-field environments while minimizing measurement back-action. These key differences, as well as the extreme difference in effective interrogation window, are summarized in Table 2.

Future improvements in frequency stability and membrane quality factors could further enhance force sensitivity, positioning this method as a versatile tool for precision-force metrology and quantum sensing. Potential applications include measurements of Casimir interactions,[1] detection of pressure or acceleration signals, and real-time monitoring of nanoscale growth processes of conducting surfaces. More broadly, integrating STM-based transduction with advanced nanomechanical platforms may enable exploration of macroscopic quantum phenomena in systems where localized, minimally invasive readouts are essential.

8. METHODS

8.1. Electronic Setup

For this study, we use a Joule−Thomson scanning tunneling microscope (JT-STM) by SPECS, equipped with optical access. The STM scanner can be cooled to ∼1 K through a combination of liquid nitrogen, liquid helium, and a Joule−Thomson cooling cycle. The STM chamber is pumped to about 10^{-10} mbar, and the shielded volume around the scanning probe reaches pressures of 10^{-11} mbar or below.

Figure 6 shows the electronic setup. A tungsten STM tip is mounted on a piezo tube controlled by the STM operating system (Nanonis). The piezo tube adjusts the tip height dynamically, either via a constant-current feedback loop or, in the case of the Z-sweep resonance modality, through controlled open-loop sweeps. In the feedback mode, the measured current is continuously compared to a set point (target) current. If the measured current falls below the set point, the operating system increases the piezo voltage, moving the tip closer to the membrane, and vice versa.

The tunneling current is low-pass filtered by a FEMTO DLPCA-200 preamplifier with a bandwidth of 1.1 kHz, providing a transimpedance gain of 10^9 V/A. This bandwidth limits both the response speed of the feedback loop and our ability to resolve the membrane's true mechanical motion in real time, but it allows us to measure currents with pA precision.

STM electronics apply a steady DC bias voltage, which maintains the tunneling current and can be used to adjust the chemical potential (Figure 3). An RF generator (Rohde and Schwarz SMB100A) provides an AC excitation in the range of 100 kHz to 1 MHz. The DC and AC signals are combined with a bias tee (Mini-Circuits ZFBT-4R2GW+) and routed to the sample holder through the JT-STM wiring.

The sample holder is made of molybdenum with tantalum clips securing the experimental chip via molybdenum screws. Because the chip includes two insulating layers (illustrated in blue in Figure 6), the electrical signal is routed only to the top surface through the tantalum clips, ensuring that the AC and DC voltages couple to the membrane. Figure 6 illustrates the configuration for the NbTiN-coated membrane; an otherwise identical gold-coated chip is described in the Section 8.4.

Throughout the experiment, the AC signal was chopped using the internal modulation feature of the RF generator, with a duty cycle of 50% and a modulation frequency $f_{LI} \leq 1.1$ kHz. This chopping effectively reduces the time-averaged applied power by 3 dB. The RF generator also provides a trigger reference to a lock-in amplifier (Stanford Research SR830), which demodulates the low-pass-filtered tunnel current and thereby measures the difference between RF-on and RF-off phases. We kept the chopping enabled even in measurements where no homodyne detection signal was recorded, as it did not adversely affect the other modalities. One example of a combined data set between homodyne detection and feedback resonance is shown in Supplementary Note 5.

8.2. Mathematical Model

Here, we expand upon the mathematical description provided in the main text. We consider the fundamental mode of the membrane with the generalized coordinate r, which measures the membrane displacement relative to its equilibrium position. In addition to the intrinsic harmonic restoring force, the membrane experiences an interaction with the STM tip, dominated by Lennard-Jones and electrostatic contributions (see Figure 2a). In the absence of tip−sample interactions, the membrane behaves as a harmonic oscillator of stiffness k. Including the tip-induced interactions, the total potential energy of the system can be expressed as

Downloaded from http://pubs.acs.org/ancac3/article-pdf/20/28/20160/6530070/acsnano.6c04148.pdf by TU DELFT user on 29 July 2026

https://doi.org/10.1021/acsnano.6c04148
ACS Nano 2026, 20, 20160−20175

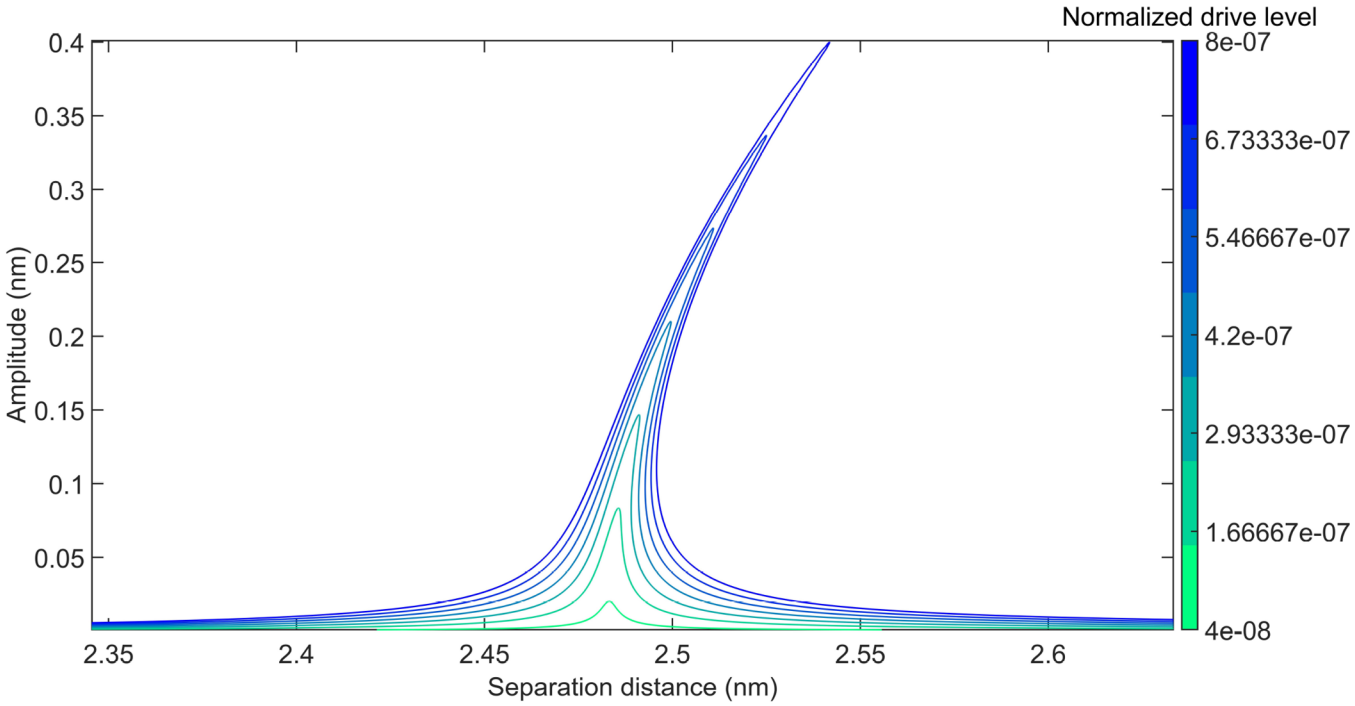


Figure 7. Numerical continuation simulations. Steady-state oscillation amplitude as a function of tip−membrane separation distance for a fixed drive frequency $w_d/2\pi$ = 277.77 kHz. Curves correspond to different normalized drive levels (color scale). The simulations illustrate the nonlinear response and emergence of multivalued solutions near resonance.

$$U(r) = \frac{1}{2}kr^2 + 4\epsilon_{LJ}\left[\left(\frac{\sigma}{r+d}\right)^{12} - \left(\frac{\sigma}{r+d}\right)^{6}\right] - \frac{C_1V_{DC}^2}{r+d} \tag{3}$$

Here, the electrostatic potential is given by the last term. From this, we can derive the force $F(r) = -\frac{\partial U}{\partial r}$ imparted by the tip on a static membrane as

$$F(d, V_{DC}) = 4\epsilon_{LJ}\left[-12\left(\frac{\sigma^{12}}{d^{13}}\right) + 6\left(\frac{\sigma^6}{d^7}\right)\right] - \frac{C_1V_{DC}^2}{d^2} \tag{4}$$

Assuming modal mass m and kinetic energy $T = \frac{1}{2}m\dot{r}^2$, we can express the Lagrangian as $\mathcal{L} = T - U$, which results in the following Lagrange equation of motion, $\frac{d}{dt}\left(\frac{\partial \mathcal{L}}{\partial \dot{r}}\right) - \frac{\partial \mathcal{L}}{\partial r} = 0$:

$$m\ddot{r} + kr + 4\epsilon_{LJ}\left(-12\frac{\sigma^{12}}{(r+d)^{13}} + 6\frac{\sigma^6}{(r+d)^7}\right) + \frac{C_1V_c^2}{(r+d)^2} = 0 \tag{5}$$

The effective resonance frequency of the mode can be approximated by taking the first-order Taylor expansion of the forces around $r = 0$, resulting in the effective linear stiffness k_{eff} and effective resonance frequency ω_{eff}:

$$k_{eff} = k + 4\epsilon_{LJ}\left(\frac{156\sigma^{12}}{d_0^{14}} - \frac{42\sigma^6}{d^8}\right) - \frac{2C_1V_c^2}{d^3} \tag{6}$$

$$\omega_{eff} = \sqrt{\frac{k_{eff}}{m}} = \sqrt{\omega_0^2 + \frac{4\epsilon_{LJ}}{m}\left(\frac{156\sigma^{12}}{d^{14}} - \frac{42\sigma^6}{d^8}\right) - \frac{2C_1V_c^2}{md^3}} \tag{7}$$

where ω_0 is the linear resonance frequency. The shift of the resonance frequency squared can be conveniently expressed as

$$\Delta\omega^2 = \omega_{eff}^2 - \omega_0^2 = \frac{4\epsilon_{LJ}}{m}\left(\frac{156\sigma^{12}}{d^{14}} - \frac{42\sigma^6}{d^8}\right) - \frac{2C_1V_c^2}{md^3} \tag{8}$$

Thus

$$\Delta f^2 = \frac{1}{4\pi^2}\left[\frac{4\epsilon_{LJ}}{m}\left(\frac{156\sigma^{12}}{d^{14}} - \frac{42\sigma^6}{d^8}\right) - \frac{2C_1V_{DC}^2}{md^3}\right] \tag{9}$$

This expression corresponds to the special case $p = 2$ of the phenomenological electrostatic force introduced in the main text. During the fit of Figure 5a, a generalized power-law dependence $F_{ES} \propto V_{DC}^2/d^p$ is employed, and the best agreement with the measured frequency shifts is obtained for $p \simeq 2$, corresponding to a force-gradient scaling $\partial_d F_{ES} \propto d^{-3}$. This corresponds with a sharp tip.

After extracting the coefficients from a fit, we can then simulate the following equation of motion using numerical continuation[31] in order to obtain the nonlinear steady-state response of the driven system:

$$\ddot{r} + \omega_0^2 r + \frac{\omega_0}{Q}\dot{r} - \frac{4\epsilon_{LJ}}{m}\left(-12\frac{\sigma^{12}}{(r+d)^{13}} + 6\frac{\sigma^6}{(r+d)^7}\right) + \frac{C_1V_{DC}^2}{m(r+d)^2} = F_d\cos\omega_d t \tag{10}$$

where F_d is the drive level and ω_d is the drive frequency. We use a Q-factor of $Q = 10^6$, in line with the experiments, and a set of drive levels F_d according to the shifts of nonlinear resonance peaks with respect to the separation distance in the experiments. By setting different drive frequencies, we execute numerical continuation with separation distance, d, as the continuation parameter. This is done in order to simulate the Z-sweep resonance modality.

Numerical continuation simulations (Figure 7) reveal multiple solutions for the steady state of the system at high drive levels due to the nonlinear softening effect, similar to what happens in a Duffing oscillator. As the separation distance is increased during a Z-sweep resonance curve, it effectively increases the linear resonance frequency, while the drive frequency is kept the same. This effectively imitates a frequency sweep in a reverse fashion (which is why we observe a shape similar to nonlinear hardening frequency response instead of a softening shape, in Figure 7). The amplitudes found in the figure are added on top of the separation distance to help determine the effective distance for tunneling, allowing the curves in

Downloaded from http://pubs.acs.org/ancac3/article-pdf/20/28/20160/6530070/acsnano.6c04148.pdf by TU DELFT user on 29 July 2026

https://doi.org/10.1021/acsnano.6c04148
ACS Nano 2026, 20, 20160−20175

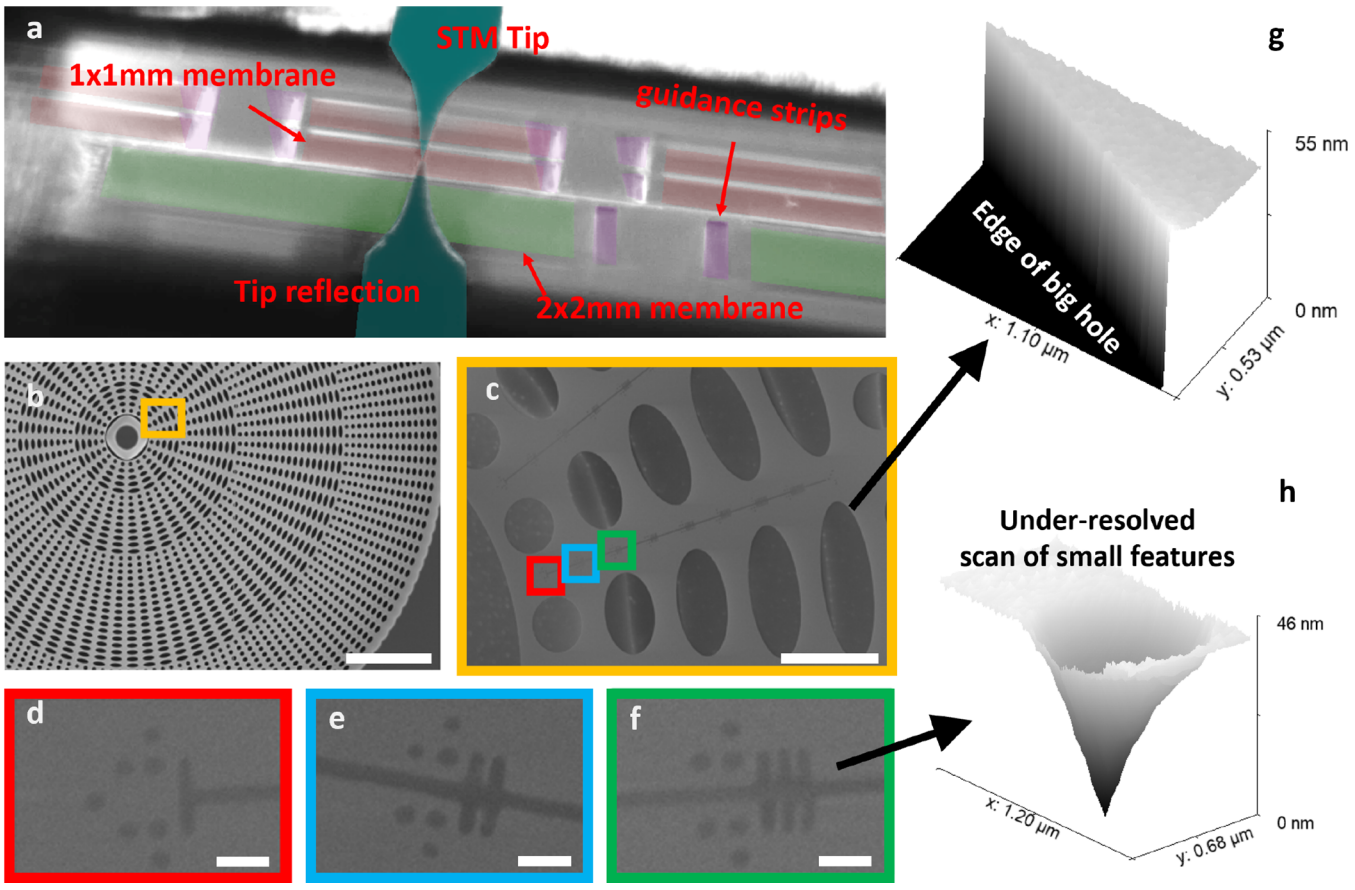


Figure 8. Navigation system. (a) Optical image of the tip−sample junction, using false-color overlays for identification of various parts. (b) Scanning electron microscopy (SEM) image of the membrane showing large underetch holes and smaller marker holes used for navigation, with a magnified view in (c) and further enlargements in (d−f). (g) STM topographic scan of a large hole. The measured depth reaches 55 nm, corresponding to the maximum tip extension during this scan; no tunneling current was detected at the bottom, indicating that the true hole depth exceeds the measured value. (h) STM scan of a marker hole. The feature appears broadened due to limited lateral resolution under the given tip conditions. The scale bar in panel b is 40 μm, in panel c it is 4 μm, and in panels d−f it is 200 nm.

Figure 2 to be established. As shown in Supporting Information Note 9, a significant part of the current flows during the maximum extension of the oscillation.

8.3. Membrane Navigation System

The insets shown in Figure 4c−e are made possible thanks to optical access. Figure 8a shows such an image in more detail, highlighting an STM tip approaching from the top. A reflection of the tip aids in locating the probing point, with guiding strips on each membrane's side. Highlighted is also a 2 × 2 mm gold-coated membrane suspended over a gold-coated Si chip. The tip is shown probing a membrane coated by superconducting NbTiN on Si_3N_4. The two chips are placed firmly next to each other, allowing us to probe both types of membranes within a single experimental cycle.

In earlier iterations of the experiment, an attempt was made at measuring the absolute out-of-plane motion of a membrane. To this end, a membrane was made with a hole in the middle in which a pedestal was placed, such that the STM tip would measure the height difference between the pedestal and the oscillating membrane. In order to find this micrometer-sized pedestal, an on-membrane navigation system was implemented; see Figure 8b−f. As with the membrane in this main work (see the Section 8.4), these earlier membranes had holes that helped with plasma etching. However, they served a double function as a navigation system. The holes were laid out concentrically around the pedestal, with an elliptical shape, the exact details of which depend on the relative distance and angle from the pedestal.

Additional markers with unique shapes were made to be smaller than 1 × 1 μm, as shown in panels d−f, such that a single marker would fit within a single scan frame of the STM. The experimentalist would then search their scan window for any such holes, determine their shape, and deduce where to move from there. Due to the tip's apex shape, the smaller markers were not properly resolved but appeared as elliptic depressions (panel h). The large holes (used for underetching), on the other hand, resulted in a very large and very sudden height change (panel g). This allowed us to distinguish between both types of holes and helped guide us toward the center of the membrane.

We did not optimize the tip apex to properly resolve the small markers. We expect STM tips that are prepared more carefully, such as through a combination of field ion microscopy (FIM) and field emission microscopy (FEM), to benefit more from this navigation system.[32,33]

8.4. Sample Preparation

8.4.1. Fabrication of the 2 × 2 mm^2 Silicon Nitride (Si_3N_4) Mechanical Resonator Coated with Gold. A 340 nm Si_3N_4 film with 1.1 GPa tensile stress is deposited by low-pressure chemical vapor deposition (LPCVD) on a silicon wafer. The wafer is diced into 10 × 10 mm^2 chips. On a microchip, a square array of circular holes with radius 0.75 μm and center-to-center distance 3.5 μm in both x and y directions is patterned on the Si_3N_4 film. The circular holes are patterned by using electron-beam lithography on a positive tone e-beam resist (AR-P 6200) and subsequently transferred to the Si_3N_4 layer using inductively coupled plasma reactive ion etching (ICP-RIE) based on CHF_3 and argon plasmas. The residual resist is removed by hot dimethylformamide (DMF). Then, the 2 × 2 mm^2 nano-mechanical squared membranes are released by cryogenic SF_6

https://doi.org/10.1021/acsnano.6c04148
ACS Nano 2026, 20, 20160−20175

Downloaded from http://pubs.acs.org/ancac3/article-pdf/20/28/20160/6530070/acsnano.6c04148.pdf by TU DELFT user on 29 July 2026

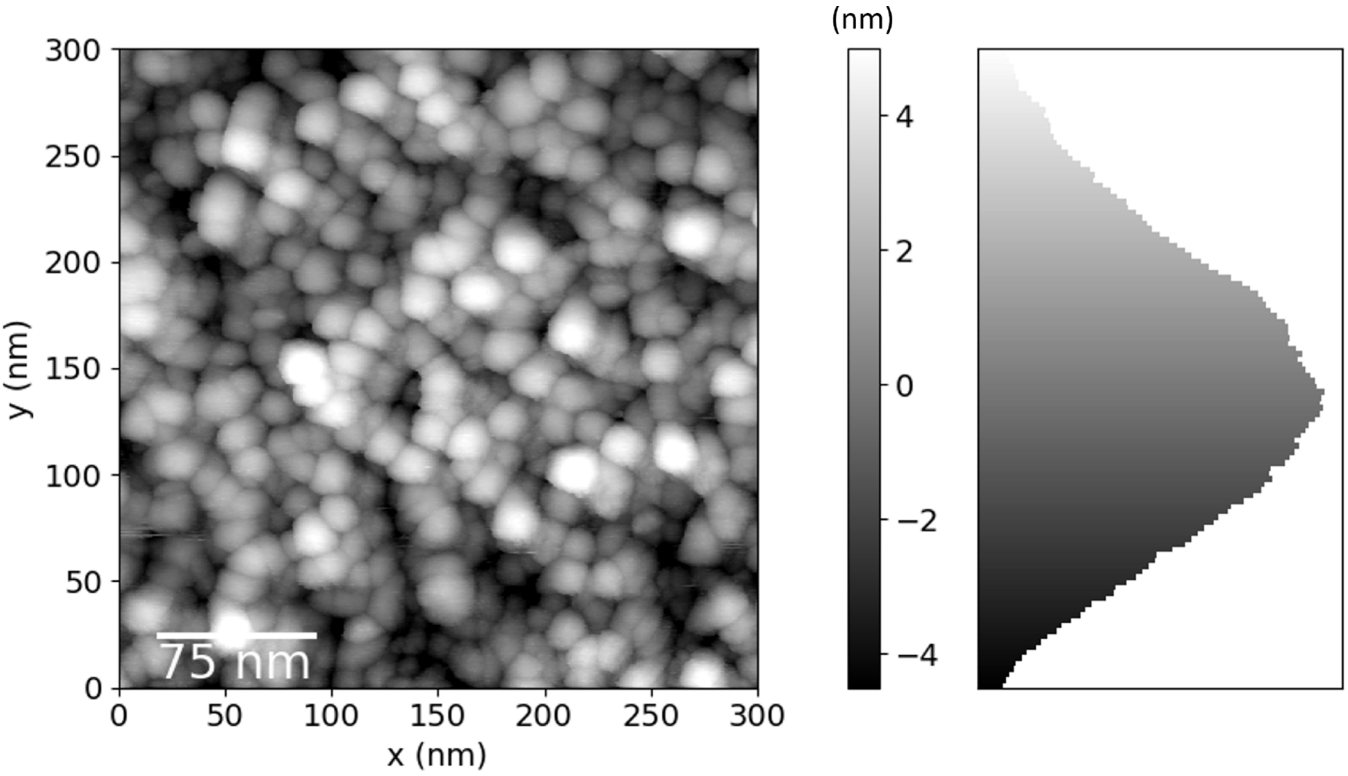


Figure 9. Sample topography. A topographic scan of 300 × 300 nm^2 of the Nb-coated membrane, showing a surface with a grain-like cover. Typical grain size is roughly 20 nm. The color bar shown on the right is on the order of several nanometers, with the histogram indicating a standard deviation of 2.1 nm.

isotropic plasma etching of the Si substrate using ICP etching at −120 °C. Finally, a 45 nm gold film is coated on the suspended membrane, using thermal evaporation. In between the Si_3N_4 and gold films, a 2 nm thin chromium adhesive layer is added for coating.

Figure 9 presents a typical topography of the Nb-coated membrane showing grains with a typical grain size of 20 nm. From the histogram of the measured heights (right), we determined a standard deviation of 2.1 nm, which we take as a measure for the roughness of the surface.

8.4.2. Fabrication of the 1 × 1 mm^2 Si_3N_4 Mechanical Resonator Coated with Niobium Titanium Nitride (NbTiN). On a microchip coated with a 340 nm thick Si_3N_4 deposited as described above, a 45 nm thick NbTiN layer is coated on it at 300 °C using plasma-enhanced atomic layer deposition (PEALD). Then we pattern the circular holes in the same way as described above, except that the array has a size of 1 × 1 mm^2, on the Si_3N_4/NbTiN bilayer. At last, we suspend the 1 × 1 mm^2 squared membrane using cryogenic SF_6 isotropic plasma etching to undercut the Si substrate at −120 °C.

■ ASSOCIATED CONTENT

Data Availability Statement

Open Data is publicly accessible through Zenodo on 10.5281/zenodo.18308260.

Supporting Information

The Supporting Information is available free of charge at https://pubs.acs.org/doi/10.1021/acsnano.6c04148.

Summary of experimental parameters used for the main text and supplementary figures; additional *Q*-factor measurements; scanning tunneling spectroscopy of the superconducting gap; details of the signal chopping and homodyne detection scheme; characterization of the linear-response regime, feedback oscillations, telegraphic noise, and feedback stability; measurements of local contact potential difference variations; derivations for the time-averaged tunneling current; details of the procedure used to extract z_{rise}; and additional information related to the force-sensitivity analysis (PDF)

■ AUTHOR INFORMATION

Corresponding Authors

Sander Otte − *Kavli Institute of Nanoscience, Department of Quantum Nanoscience, Delft University of Technology, Delft 2628CJ, The Netherlands;* orcid.org/0000-0003-0781-8537; Email: a.f.otte@tudelft.nl

Richard A. Norte − *Kavli Institute of Nanoscience, Department of Quantum Nanoscience, Delft University of Technology, Delft 2628CJ, The Netherlands; Department of Precision and Microsystems Engineering, Delft University of Technology, Delft 2628CD, The Netherlands;* Email: r.a.norte@tudelft.nl

Authors

Robertus J. G. Elbertse − *Kavli Institute of Nanoscience, Department of Quantum Nanoscience, Delft University of Technology, Delft 2628CJ, The Netherlands;* orcid.org/0000-0002-1429-1297

Minxing Xu − *Kavli Institute of Nanoscience, Department of Quantum Nanoscience, Delft University of Technology, Delft 2628CJ, The Netherlands; Department of Precision and Microsystems Engineering, Delft University of Technology, Delft 2628CD, The Netherlands*

Ata Keşkekler − *Department of Precision and Microsystems Engineering, Delft University of Technology, Delft 2628CD, The Netherlands*

Downloaded from http://pubs.acs.org/ancac3/article-pdf/20/28/20160/6530070/acsnano.6c04148.pdf by TU DELFT user on 29 July 2026

https://doi.org/10.1021/acsnano.6c04148
ACS Nano 2026, 20, 20160−20175

Complete contact information is available at:
https://pubs.acs.org/10.1021/acsnano.6c04148

Author Contributions

§R.J.G.E. and M.X. contributed equally to this work.

Notes

The authors declare no competing financial interest.

■ ACKNOWLEDGMENTS

We thank Martin Lee for early cleanroom support, along with Charles de Boer, Marinus Fischer, Bas van Asten, Pauline Stevic, and Roald van der Kolk. We thank Allard Katan for early ideas. This publication is part of the project "Probing the physics of exotic superconductors with microchip Casimir experiments" (740.018.020) of the research program NWO Start-up. which is partly financed by the Dutch Research Council (NWO). It was funded/co-funded by the European Union (ERC, EARS, 101042855). Views and opinions expressed are however those of the author(s) only and do not necessarily reflect those of the European Union or the European Research Council.

■ REFERENCES

(1) Xu, M.; Elbertse, R. J. G.; Keşkekler, A.; Bimonte, G.; Lee, J.; Otte, S.; Norte, R. A. Measuring Casimir Force Across a Superconducting Transition. 2025, .
(2) Thompson, J.; Zwickl, B.; Jayich, A.; Marquardt, F.; Girvin, S.; Harris, J. Strong dispersive coupling of a high-finesse cavity to a micromechanical membrane. *Nature* **2008**, *452*, 72−75.
(3) Norte, R. A.; Moura, J. P.; Gröblacher, S. Mechanical resonators for quantum optomechanics experiments at room temperature. *Phys. Rev. Lett.* **2016**, *116*, No. 147202.
(4) Reinhardt, C.; Müller, T.; Bourassa, A.; Sankey, J. C. Ultralow-Noise SiN Trampoline Resonators for Sensing and Optomechanics. *Phys. Rev. X* **2016**, *6*, No. 021001.
(5) Tsaturyan, Y.; Barg, A.; Polzik, E. S.; Schliesser, A. Ultracoherent nanomechanical resonators via soft clamping and dissipation dilution. *Nat. Nanotechnol.* **2017**, *12*, 776−783.
(6) Andrews, R. W.; Peterson, R. W.; Purdy, T. P.; Cicak, K.; Simmonds, R. W.; Regal, C. A.; Lehnert, K. W. Bidirectional and efficient conversion between microwave and optical light. *Nat. Phys.* **2014**, *10*, 321−326.
(7) Malcovati, P.; Baschirotto, A. The evolution of integrated interfaces for MEMS microphones. *Micromachines* **2018**, *9*, 323.
(8) Zawawi, S. A.; Hamzah, A. A.; Majlis, B. Y.; Mohd-Yasin, F. A review of MEMS capacitive microphones. *Micromachines* **2020**, *11*, 484.
(9) Hälg, D.; Gisler, T.; Tsaturyan, Y.; Catalini, L.; Grob, U.; Krass, M.-D.; Héritier, M.; Mattiat, H.; Thamm, A.-K.; Schirhagl, R.; Langman, E. C.; Schliesser, A.; Degen, C. L.; Eichler, A. Membrane-Based Scanning Force Microscopy. *Phys. Rev. Appl.* **2021**, *15*, No. L021001.
(10) Xu, H.; Venkatachalam, S.; Rabenimanana, T.-H.; Boyaval, C.; Eliet, S.; Braud, F.; Collin, E.; Theron, D.; Zhou, X. Imaging nanomechanical vibrations and manipulating parametric mode coupling via scanning microwave microscopy. *Nano Lett.* **2024**, *24*, 8550−8557.
(11) Uder, B.; Gao, H.; Kunnas, P.; de Jonge, N.; Hartmann, U. Low-force spectroscopy on graphene membranes by scanning tunneling microscopy. *Nanoscale* **2018**, *10*, 2148−2153.
(12) Breitwieser, R.; Hu, Y.-C.; Chao, Y. C.; Tzeng, Y. R.; Liou, S.-C.; Lin, K. C.; Chen, C. W.; Pai, W. W. Investigating ultraflexible freestanding graphene by scanning tunneling microscopy and spectroscopy. *Phys. Rev. B* **2017**, *96*, No. 085433.
(13) Alyobi, M. M.; Barnett, C. J.; Muratov, C. B.; Moroz, V.; Cobley, R. J. The voltage-dependent manipulation of few-layer graphene with a scanning tunneling microscopy tip. *Carbon* **2020**, *163*, 379−384.
(14) Zan, R.; Muryn, C.; Bangert, U.; Mattocks, P.; Wincott, P.; Vaughan, D.; Li, X.; Colombo, L.; Ruoff, R. S.; Hamilton, B.; et al. Scanning tunnelling microscopy of suspended graphene. *Nanoscale* **2012**, *4*, 3065−3068.
(15) Klimov, N. N.; Jung, S.; Zhu, S.; Li, T.; Wright, C. A.; Solares, S. D.; Newell, D. B.; Zhitenev, N. B.; Stroscio, J. A. Electromechanical properties of graphene drumheads. *Science* **2012**, *336*, 1557−1561.
(16) Xu, P.; Yang, Y.; Barber, S.; Ackerman, M.; Schoelz, J.; Qi, D.; Kornev, I. A.; Dong, L.; Bellaiche, L.; Barraza-Lopez, S.; et al. Atomic control of strain in freestanding graphene. *Phys. Rev. B—Condens. Matter Mater. Phys.* **2012**, *85*, No. 121406.
(17) Zhao, X.; Zhai, X.; Zhao, A.; Wang, B.; Hou, J. Fabrication and scanning tunneling microscopy characterization of suspended monolayer graphene on periodic Si nanopillars. *Appl. Phys. Lett.* **2013**, *102*, 201602.
(18) Breitwieser, R.; Hu, Y.-C.; Chao, Y. C.; Li, R.-J.; Tzeng, Y. R.; Li, L.-J.; Liou, S.-C.; Lin, K. C.; Chen, C. W.; Pai, W. W. Flipping nanoscale ripples of free-standing graphene using a scanning tunneling microscope tip. *Carbon* **2014**, *77*, 236−243.
(19) Schoelz, J.; Xu, P.; Meunier, V.; Kumar, P.; Neek-Amal, M.; Thibado, P.; Peeters, F. Graphene ripples as a realization of a two-dimensional Ising model: A scanning tunneling microscope study. *Phys. Rev. B* **2015**, *91*, No. 045413.
(20) Uder, B.; Hartmann, U. A convenient method for large-scale STM mapping of freestanding atomically thin conductive membranes. *Rev. Sci. Instrum.* **2017**, *88*, No. 063702.
(21) Thoen, D. J.; Bos, B. G. C.; Haalebos, E.; Klapwijk, T.; Baselmans, J.; Endo, A. Superconducting NbTin Thin Films With Highly Uniform Properties Over a 100 mm Wafer. *IEEE Transactions on Applied Superconductivity* **2017**, *27*, 1−5.
(22) Israelachvili, J. N. *Intermolecular and Surface Forces*, 3rd ed.; Academic Press: Amsterdam, 2011.
(23) Faust, T.; Rieger, J.; Seitner, M. J.; Krenn, P.; Kotthaus, J. P.; Weig, E. M. Nonadiabatic Dynamics of Two Strongly Coupled Nanomechanical Resonator Modes. *Phys. Rev. Lett.* **2012**, *109*, No. 037205.
(24) Mahboob, I.; Yamaguchi, H. Piezoelectrically pumped parametric amplification and Q enhancement in an electromechanical oscillator. *Appl. Phys. Lett.* **2008**, *92*, 173109.
(25) Elfrink, R.; Kamel, T. M.; Goedbloed, M.; Matova, S.; Hohlfeld, D.; van Andel, Y.; van Schaijk, R. Vibration energy harvesting with aluminum nitride-based piezoelectric devices. *Journal of Micromechanics and Microengineering* **2009**, *19*, No. 094005.
(26) Farah, T.; Flis, L.; Laly, P.; Chang, G.-E.; Ou, J.-Y.; Tsuchiya, Y.; Pennec, Y.; Djafari-Rouhani, B.; Zhou, X. Implementation of Reservoir Computing Using Coupled Microelectromechanical Drum Resonators via Sideband-Pumped Phonon-Cavity Dynamics. *arXiv:2601.02617*. 2026,
(27) Mu, G.; Snell, N.; Zhang, C.; Xie, X.; Tahvildari, R.; Weck, A.; Godin, M.; St-Gelais, R. Observation of Silicon Nitride Nanomechanical Resonator Actuation Using Capacitive Substrate Excitation. *arXiv:2112.09303*. 2021, .
(28) Li, J.; Zhang, Q.; Ha, S.; Demosthenous, A.; Jiang, D.; Wu, Y. A 0.62 μW/sensor 82fps Time-to-Digital Impedance Measurement IC with Unified Excitation/Readout Front-End for Large-Scale Piezo-Resistive Sensor Array. In *2026 IEEE International Solid-State Circuits Conference (ISSCC)*, 2026; pp 1−3.
(29) Hwang, J.; Krylov, D.; Elbertse, R.; Yoon, S.; Ahn, T.; Oh, J.; Fang, L.; Jang, W.-J.; Cho, F. H.; Heinrich, A. J.; Bae, Y. Development of a scanning tunneling microscope for variable temperature electron spin resonance. *Rev. Sci. Instrum.* **2022**, *93*, No. 093703.
(30) Bettac, A.; Koeble, J.; Winkler, K.; Uder, B.; Maier, M.; Feltz, A. QPlus: atomic force microscopy on single-crystal insulators with small oscillation amplitudes at 5 K. *Nanotechnology* **2009**, *20*, 264009.
(31) Doedel, E. J.; Champneys, A. R.; Dercole, F.; Fairgrieve, T. F.; Kuznetsov, Y. A.; Oldeman, B.; Paffenroth, R.; Sandstede, B.; Wang,

Downloaded from http://pubs.acs.org/ancac3/article-pdf/20/28/20160/6530070/acsnano.6c04148.pdf by TU DELFT user on 29 July 2026

X.; Zhang, C. AUTO-07P: Continuation and bifurcation software for ordinary differential equations. 2007.
(32) Gomer, R. Field Emission and Field Ionization. In *Harvard monographs in applied science*; Harvard University Press, 1961.
(33) Muller, E.; Tsong, T. *Field Ion Microscopy: Principles and Applications*; American Elsevier Publishing Company, 1969.

Downloaded from http://pubs.acs.org/ancac3/article-pdf/20/28/20160/6530070/acsnano.6c04148.pdf by TU DELFT user on 29 July 2026

https://doi.org/10.1021/acsnano.6c04148
ACS Nano 2026, 20, 20160−20175